



**HAL**  
open science

## **Analysis of index modulation in microembolic Doppler signals part I: radiation force as a new hypothesis-simulations**

Jean-Marc Girault, Denis Kouamé, Sébastien Ménigot, Grégory Souchon,  
François Tranquart

► **To cite this version:**

Jean-Marc Girault, Denis Kouamé, Sébastien Ménigot, Grégory Souchon, François Tranquart. Analysis of index modulation in microembolic Doppler signals part I: radiation force as a new hypothesis-simulations. *Ultrasound in Medicine & Biology*, 2011, 37 (1), pp.87-101. 10.1016/j.ultrasmedbio.2010.09.006 . hal-00658788

**HAL Id: hal-00658788**

**<https://hal.science/hal-00658788>**

Submitted on 11 Jan 2012

**HAL** is a multi-disciplinary open access archive for the deposit and dissemination of scientific research documents, whether they are published or not. The documents may come from teaching and research institutions in France or abroad, or from public or private research centers.

L'archive ouverte pluridisciplinaire **HAL**, est destinée au dépôt et à la diffusion de documents scientifiques de niveau recherche, publiés ou non, émanant des établissements d'enseignement et de recherche français ou étrangers, des laboratoires publics ou privés.

# Analysis of Index Modulation in microembolic Doppler signals Part I: Radiation Force as a new hypothesis - simulations

Jean-Marc Girault,<sup>a</sup> Denis Kouamé,<sup>b</sup> Sébastien Ménigot,<sup>a</sup>

Grégory Souchon,<sup>a</sup> François Tranquart<sup>c</sup>

<sup>a</sup>*Université François Rabelais de Tours, UMRS "Imaging and Brain" U930 and CNRS ERL  
3106, Tours, France.*

<sup>b</sup>*Université PAUL Sabatier de Toulouse 3, IRIT UMR 5505, France*

<sup>c</sup>*Bracco, Switzerland*

Corresponding Author: Jean-Marc Girault

Inserm U930 - CNRS ERL 3106 - Équipe 5

UFR de Médecine

10 boulevard Tonnellé, BP3223

F-37032 TOURS CEDEX 1

Email: jean-marc.girault@univ-tours.fr

Telephone: +33 (0)2 47 36 62 21

Elsevier

Ultrasound in Medicine & Biology, Volume 37, Issue 1, January 2011, Pages 87-101

DOI : 10.1016/j.ultrasmedbio.2010.09.006

<http://www.sciencedirect.com/science/article/pii/S0301562910005028>

## Abstract

The purpose of this study was to reveal the cause of frequency modulation (FM) present in microembolic Doppler ultrasound signals. This novel explanation should help the development of sensitive microembolus discrimination techniques. We suggest that the frequency modulation detected is due to the ultrasonic radiation force (URF) acting directly on microemboli. The frequency modulation and the imposed displacement were calculated using a numerical dynamic model. By setting simulation parameters with practical values, it was possible to reproduce most microembolic frequency modulation signatures (FMS). The most interesting findings in this study were that: 1) the ultrasound radiation force acting on a gaseous microembolus and its corresponding cumulative displacement were far higher than those obtained for a solid microembolus, and that is encouraging for discrimination purposes, and 2) the calculated frequency modulation indices (FMI) ( $\approx 20$  kHz) were in good agreement with literature results. By taking into account the ultrasound radiation force, the flow pulsatility, the beam-to-flow angle and both the velocity and the US beam profiles, it was possible to explain all erratic FM signatures of a microbubble. Finally, by measuring FMI from simulated Doppler signals and by using a constant threshold of 1 KHz, it was possible to discriminate gaseous from solid microemboli with ease.

*Key words:* Discrimination, Microemboli, ultrasound radiation force, frequency modulation signature.

## 1 Introduction

2 Cerebral embolisms represent a significant proportion of all ischemic strokes in western  
3 countries, and identification of types of microemboli (gaseous or solid) and size may be  
4 important for diagnosis and subsequent treatment. The Transcranial Doppler (TCD) sys-  
5 tem is the most commonly used method for microembolus detection, and time-frequency  
6 representation provides valuable indications (frequency modulation) of the nature and  
7 size of a microembolus.

8 Many reports have been published concerning the differentiation of gaseous and particu-  
9 late matter ((Russell et al., 1991; Markus and Brown, 1993; Georgiadis et al., 1994; Smith  
10 et al., 1997, 1998; Russell and Brucher, 2002)). Some of them have focused on the measure-  
11 ment of microembolus velocity or duration (Markus and Brown, 1993; Georgiadis et al.,  
12 1994; Russell and Brucher, 2002), and others on the measurement of the microembolic  
13 signal (MES) intensity (Markus and Brown, 1993; Smith et al., 1997). In practice, when  
14 a TCD system detects high intensity transient signals (HITS) many interpretations are  
15 possible based on the scattering theory: they may be due to a small gaseous microembolus  
16 (a few microns) such as from a prosthetic heart valve, a small formed element (tens of  
17 microns) such as from prosthetic a heart valve or an arterial lesion with ulceration, a large  
18 bubble such as from air trapped in the vasculature during surgery, or a large piece of clot  
19 such as from atrial fibrillation. Hence, most of the parameters used for discrimination  
20 implemented in on- or off-line systems are based on the linearity of the backscattered  
21 Doppler signal. The most popular are embolic duration (ED) (Markus and Brown, 1993;  
22 Smith et al., 1997), embolic velocity (EV) (Smith et al., 1997), embolus to blood ratio  
23 (EBR) (Markus and Brown, 1993; Smith et al., 1997; Russell and Brucher, 2002), signal to  
24 error ratio (SER) (Devuyst et al., 2000), frequency band and symmetry of the HITS sig-  
25 nature (Devuyst et al., 2001) and sample volume length (SVL) (Smith et al., 1998). How-  
26 ever, the parameter which seems to us the most interesting and relevant is the frequency  
27 modulation index (FMI) (Smith et al., 1997). This parameter, which measures the slope

28 intensity of the microembolic frequency modulation signature (FMS), is important since  
29 it is based on measuring the trajectory modification of microembolus circulation in the  
30 blood stream. The physical phenomenon which underlies this "additional-displacement"  
31 has not been clearly identified and we believe that discovering the correct explanation  
32 should lead researchers to propose more sensitive discrimination techniques.

33 The starting point of our study was the article written by Smith et al. (1997). The most  
34 remarkable finding of this study was that known solid microemboli never appear to give  
35 rise to Doppler MES with rapidly changing frequency modulations (FM). In our opin-  
36 ion this study is one of the most interesting for two reasons. First because it is based  
37 on an extensive clinical study and second because several valuable explanations are pro-  
38 posed. The clinical studies of Smith et al. (1997) and those referenced in the same article  
39 showed that the Doppler MES from patients with a prosthetic heart valve present a high  
40 frequency modulation index (FMI) whereas the FMI is low in patients with atheroscle-  
41 rotic plaques. An *in vitro* study reported by Souchon et al. (2005) confirmed that gaseous  
42 microemboli produced higher FMI than those produced by solid microemboli. Smith et al.  
43 (1997) proposed some new and valuable hypotheses such as artery curvature, helical flow,  
44 harmonic generation and phase cancelation to explain the different types of FM. Further-  
45 more, Smith et al. (1997) proposed three distinct types of FM: those with no modulation  
46 (type I), those with gradual FM observed over the majority of the signal duration (type  
47 II) and those with a rapid change evident in only a small percentage of the entire signal  
48 duration (type III). The most surprising type III FM signatures observed in the time-  
49 frequency domain resemble a "V" shape or a reversed "V" shape. We propose here a valid  
50 explanation for these strange signatures.

51 The aim of the present study was to extend the results of Smith et al. (1997). To explain  
52 the three types of FM, we hypothesized that the major physical phenomenon involved in  
53 the modification of the microembolus trajectory is the ultrasound radiation force (URF)  
54 and therefore studied many aspects. Many factors were studied to prove that the URF  
55 explains these strange FMS. First, the necessary background physics are reviewed, and

56 the dynamics of a microembolus crossing an ultrasound beam are examined. A numeri-  
57 cal simulation based on different models is then introduced to calculate the theoretical  
58 values of both the URF and the microdisplacement. Finally, different types of FMS cal-  
59 culated from simulated Doppler microembolic signals are discussed and several valuable  
60 explanations are proposed.

## 61 **Materials and Methods**

62 Theoretical models and equations which explain how a microembolus in a circulating  
63 fluid can be displaced by a radiation force are presented in this section. After recalling  
64 Newton's law to describe the different movements, the different forces acting on the  
65 circulating microemboli (see Fig.1) are taken into consideration, and the drag force and  
66 the radiation force are introduced. Finally, a numerical model is discussed which predicts  
67 the modification of the microembolus trajectory .

### 68 *Newton's law*

69 The "additional displacement" (or rather the "additional acceleration") of a microembo-  
70 lus due to the radiation force is governed by Newton's law. This is an additional accel-  
71 eration to the natural acceleration induced by the spatiotemporal blood flow in which the  
72 microembolus is circulating. Newton's law is written:

$$73 \quad \sum \vec{F} = \vec{F}_{US} + \vec{F}_{DG} = \tilde{m} \vec{\gamma}, \quad (1)$$

74 where  $\tilde{m}$  corresponds to the mass of the microembolus and  $\gamma$  is the acceleration. In the  
75 case of gaseous microemboli, the effective mass corresponds to the fluid mass displaced,  
76 the effective mass here being set at 0.5 times the mass surrounding the displaced fluid  
77 (Leighton, 1994). The forces acting on the micro embolus are the drag force  $\vec{F}_{DG}$  and the  
78 radiation force  $\vec{F}_{US}$  (gravity being disregarded). As can be seen in the following section,

79 the drag force is closely related to the properties of the circulating fluid while the radiation  
 80 force is principally related to the US field.

81 *Drag force*

82 Drag force occurs when there is a relative velocity between a particle and the viscous fluid  
 83 in which the particle is immersed. When a microembolus is subjected to the radiation  
 84 force, the latter accelerates according to Newton's law. The acceleration induces a non-  
 85 negligible relative velocity between the microembolus and the fluid, which induces a drag  
 86 force.

87 For a Newtonian fluid, Benocci et al. (1986) (in the case of a gas-droplet in industrial  
 88 flow) and Tortoli et al. (2000) (in the case of contrast agent circulating in blood) proposed  
 89 a drag force model acting on a spherical microembolus (with a radius  $R_0$ ) expressed as  
 90 follows:

$$91 \quad F_{DG} = F'_{DG} \frac{C_D Re}{24} \rho, \quad (2)$$

92 where  $F'_{DG}$  is the drag force in the case of laminar flow,  $\rho$  is the density of the host fluid,  
 93 and  $Re$  and  $C_D$  are the Reynolds number and the drag coefficient, respectively. These  
 94 parameters are expressed by:

$$95 \quad \begin{aligned} F'_{DG} &= \frac{3}{2} \pi R_0 \eta \| V_f - V_b \|, \\ Re &= \frac{\| V_f - V_b \|}{\eta}, \\ C_D &= \frac{24}{Re} + \frac{6}{1 + \sqrt{Re}} + 0.4, \end{aligned} \quad (3)$$

96 where  $\eta$  is the fluid viscosity,  $R_0$  is the radius of the microembolus, and  $V_f$  and  $V_b$  are  
 97 the fluid and microembolus velocities, respectively.

98 We emphasize that this force is strongly dependent on the spatial velocity distribution

99 (laminar or plug profile) and on the heartbeat (systolic or diastolic phase). The effects of  
 100 spatial velocity distribution will be discussed later.

### 101 *Radiation Force*

102 The acoustic radiation pressure on rigid spheres freely suspended in a fluid was first calcu-  
 103 lated by King (1934). Yosioka and Kawasima (1955) extended King's results to spheres of  
 104 finite compressibility suspended in a non-viscous fluid. Doinikov (1996, 1997a,b,c, 1998)  
 105 extended the Yosioka and Kawasima model by taking thermal and viscous phenomena  
 106 into account. The latter theory is therefore appropriate to study the radiation force acting  
 107 on microemboli composed of fat or clots or even an air microbubble in a viscous fluid  
 108 (e.g. blood).

109 We examine below simplified models of radiation force acting first on a solid microembolus  
 110 and then on a gaseous microembolus. These two models, that are valid for microemboli  
 111 smaller than the wavelength, are derived from a general model which is not presented  
 112 here.

### 113 *Radiation force of a solid microembolus*

114 Assuming a small "solid" microembolus (i.e. soft material such as fat or blood clot)  
 115 suspended in plasma, the radiation force provided by the simplified Doinikov (1996)  
 116 model was reformulated as follows:

$$117 \quad F_{US} = \frac{2\pi P^2 R_0}{\rho c \omega} (R_0 k)^2 \left( \frac{3\delta_v}{R_0} \left( \frac{1 - \tilde{\rho}/\rho}{1 + 2\tilde{\rho}/\rho} \right)^2 + \frac{\delta_t}{R_0} \frac{(\nu - 1)}{2(1 + \tilde{\delta}_t \kappa / (\delta_t \tilde{\kappa}))} \right), \quad (4)$$

118 where  $P$  is the pressure level and  $\tilde{\rho}$  and  $\rho$  are the density of the microembolus and the  
 119 plasma, respectively. For this application, where the emitting wavelength is much larger  
 120 than the radius of the microembolus  $((kR_0)^2 \ll 1, (\tilde{k}R_0)^2 \ll 1$ , where  $\tilde{k} = \omega/\tilde{c}$  and  
 121  $k = \omega/c$  are the wave numbers of the microembolus and the plasma, respectively,  $\omega$  is the

122 emitting angular frequency, and  $\tilde{c}$  and  $c$  are the speed of sound within the microembolus  
123 and the plasma, respectively), the models presented are valid for a size range below  
124  $100\mu\text{m}$  when the transmitted frequency  $f = \omega/2\pi$  is 2 MHz. The depth of penetration  
125 of the viscous wave in the plasma is defined by  $\delta_v = \sqrt{2\eta/\rho/\omega}$  and the viscosity is  $\eta$ .  
126 The depth of penetration of the thermal wave in the plasma is defined by  $\delta_t = \sqrt{2\chi/\omega}$   
127 and  $\chi$  is the thermal diffusivity.  $\nu$  and  $\tilde{\nu}$  are the specific heat ratio of the plasma and the  
128 microembolus, respectively.  $\kappa$  and  $\tilde{\kappa}$  are the thermal conductivity of the plasma and the  
129 microembolus, respectively.

### 130 *Radiation force of a gaseous embolus*

131 Assuming a small gaseous microembolus suspended in plasma, the simplified Doinikov  
132 (1998) model was reformulated as follows:

$$133 \quad F_{US} = \frac{2\pi P^2 R_0}{\rho c \omega} \frac{\left(\frac{2\beta_{tot}}{\omega}\right) K}{\left(\left(\frac{\omega'_0}{\omega}\right)^2 - 1\right)^2 + \left(\frac{2\beta_{tot}}{\omega}\right)^2}. \quad (5)$$

134 When  $K = 1$  the model was equivalent to those proposed by Leighton (1994) and Dayton  
135 et al. (1997), and total damping  $\beta_{tot}$  was defined by:

$$136 \quad \beta_{tot} = \beta_{ac} + \beta_{vis} + \beta_{th}, \quad (6)$$

137 where the acoustic damping  $\beta_{ac}$ , the viscous damping  $\beta_{vis}$ , and the thermal damping  $\beta_{th}$   
138 defined by :

$$\begin{aligned} \beta_{ac} &= \frac{\omega}{2} (kR_0), \\ 139 \quad \beta_{vis} &= \frac{\omega}{2} \left(\frac{4\eta}{\omega\rho R_0^2}\right), \\ \beta_{th} &= \frac{\omega}{2} \left(\frac{\omega_0^2}{\omega^2} \frac{3(\tilde{\nu}-1)}{2R_0}\right), \end{aligned} \quad (7)$$

140 were very similar to those presented by Prosperetti (1977), Asaki and Marston (1994).

141 The resonance angular frequency  $\omega'_0$  was expressed as follows:

$$142 \quad \omega'_0 = \omega_0 \sqrt{K_2}, \quad (8)$$

143 where  $\omega_0$  is the resonance angular frequency when the surface tension  $\tilde{\sigma}$  is zero. This

144 resonance angular frequency was defined by :

$$145 \quad \omega_0 = \sqrt{\frac{3\tilde{\nu}\tilde{p}_0}{R_0^2\rho}}, \quad (9)$$

146 where  $\tilde{p}_0$  was the hydrostatic pressure and where  $\tilde{\nu}\tilde{p}_0 = \tilde{\rho}\tilde{c}^2$ . The weighted coefficients

147 presented in eqn (5) are :

$$148 \quad \begin{aligned} K &= \frac{\beta_{ac}(K_0-1)+\beta_{vis}(K_1-1)+\beta_{th}(K_2-1)}{\beta_{tot}}, \\ K_0 &= 2 + \frac{\beta_{vis}+\beta_{th}}{\beta_{ac}}, \\ K_1 &= \frac{7}{4} - \frac{3}{4} \left(\frac{\omega'_0}{\omega}\right)^2, \\ K_2 &= \frac{\omega_0'^2}{\omega_0^2} = 1 - \frac{2\tilde{\sigma}}{3R_0\tilde{\rho}\tilde{c}^2}. \end{aligned} \quad (10)$$

149 These coefficients are adimensional.

### 150 *Microembolus trajectory*

151 In this section we present the validation of the feasibility of a differentiation method

152 based on radiation force, using the numerical model initially developed by Tortoli et al.

153 (2000) and used by Palanchon et al. (2005) to estimate the displacement of microbubbles

154 crossing an ultrasound beam in an experimental setup.

155 The orthogonal projections of the radiation and drag forces on the  $\vec{r}$  and  $\vec{z}$  axis (see

156 Fig.1) provided:

$$157 \quad \begin{cases} -F_{USr} + F_{DGz}(t) = \tilde{m} \frac{dV_{br}(t)}{dt}, \\ F_{USz} - F_{DGz}(t) = \tilde{m} \frac{dV_{bz}(t)}{dt}, \end{cases} \quad (11)$$

158 where  $\tilde{m}$  represents the mass of the microembolus. The component of the drag force was  
 159 computed by splitting the relative velocity  $\|V_f - V_b\|$  into the two radial and longitudinal  
 160 components (see Fig.1). As suggested by Tortoli et al. (2000), the Euler one-step method  
 161 was used to obtain discrete forms of eqn.(11) as:

$$162 \quad \begin{cases} -F_{USr} + F_{DGz}(n) = \tilde{m} \frac{V_{br}(n+1) - V_{br}(n)}{dt}, \\ F_{USz} - F_{DGz}(n) = \tilde{m} \frac{V_{bz}(n+1) - V_{bz}(n)}{dt}. \end{cases} \quad (12)$$

163 The velocity components are thus computed as:

$$164 \quad \begin{cases} V_{br}(n+1) = \frac{-F_{USr} + F_{DGz}(n)}{\tilde{m}} dt + V_{br}(n), \\ V_{bz}(n+1) = \frac{F_{USz} - F_{DGz}(n)}{\tilde{m}} dt + V_{bz}(n). \end{cases} \quad (13)$$

165 Definition of the Lagrangian velocity makes it possible to compute the trajectory of the  
 166 microembolus in each direction as:

$$167 \quad \begin{cases} \Delta_r(n+1) = V_{br}(n).dt + \Delta_r(n), \\ \Delta_z(n+1) = V_{bz}(n).dt + \Delta_z(n). \end{cases} \quad (14)$$

168 The cumulative displacement was defined by  $\Delta_D = \sqrt{\Delta_r^2 + \Delta_z^2}$  and the elementary dis-  
 169 placement defined by  $\delta_D = \sqrt{\delta_r^2 + \delta_z^2}$  where:

$$170 \quad \begin{cases} \delta_r(n+1) = \Delta_r(n+1) - \Delta_r(n), \\ \delta_z(n+1) = \Delta_z(n+1) - \Delta_z(n). \end{cases} \quad (15)$$

171 Eqns (14), (15) were computed with Matlab (Mathworks, Natick, MA). The various  
 172 stages that we followed to calculate the trajectories of microemboli were as follows: first  
 173 we calculated the radiation force acting on the microembolus from the two models pre-  
 174 sented for gaseous and solid microemboli and then we calculated the trajectories. From  
 175 these trajectories we evaluated the cumulative displacement  $\Delta_D$ . Note that with regard  
 176 to the cumulative displacement,  $\Delta_r$  was always less than  $\Delta_z$ . Indeed,  $\Delta_z = \Delta_z^R + \Delta_z^V$   
 177 where  $\Delta_z^R$  corresponded to displacement due only to the radiation force and  $\Delta_z^V$  corre-  
 178 sponded to displacement due only to the microembolus velocity, whereas  $\Delta_r = \Delta_r^R$ . In  
 179 the case of a plug profile and without ultrasound,  $\Delta_z^V = L$ . For a fluid velocity of a  
 180 few centimeters per second,  $\Delta_D \approx \Delta_z^V$ , since  $\Delta_z^V$  was masked by  $\Delta_z^R$ . Consequently, in  
 181 order to reveal the influence of the radiation force, we preferred subsequently to calculate  
 182  $\Delta_D^* = \sqrt{\Delta_r^2 + (\Delta_z - L)^2}$ . The trajectory calculation ceased when the microembolus went  
 183 out of the US beam ( $\Delta_z > L$ , where  $L$  is the beam width) or out of the artery. Note that  
 184 the beam width seen by the microembolus was:  $L = L_{beam}/\sin\theta$ . Note that as in practice  
 185 the beam-to-flow angle is near 0 degrees, the beam width seen by the microembolus was  
 186 much higher. For instance, for  $\theta = 5$  degrees the beam width was  $L \approx 23$  mm. In practice  
 187 the ultrasound beam intersection with the middle cerebral artery (MCA) is wide since  
 188 the blood flow is mainly parallel to the ultrasound beam axis.

189 In simulations, an angle of 5 degrees was chosen because it ensures an US beam quasi  
 190 parallel to the MCA and it guarantees a reasonable computing time (the lower the angle,  
 191 the longer the computing time).

192 Since microembolus displacement is dependent on the radiation force, the drag force, the  
 193 acoustic pressure and the fluid velocity (through eqn (13) to eqn (15)), the shape of the  
 194 ultrasound beam, the velocity profile in the artery and the flow pulsatility are also factors  
 195 which significantly influence the phenomenon.

196 To observe the effects of the shape of the velocity profile we used two configurations for  
 197 which the US beam was considered as uniform, though the uniform US beam is not a

198 realistic hypothesis. However it makes it possible to reveal variations in the velocity alone.  
199 In the first configuration, the velocity profile was a plug type, *i.e.* the flow velocity on  
200 the  $\vec{z}$  axis was equal regardless of the radial position. In the second, the velocity profile  
201 was laminar, with the maximum velocity between 0.1 and 1.0 m/s (velocity range usually  
202 measured in adult cerebral arteries).

203 Similarly, to observe the effects of the shape of the ultrasound beam, we used two config-  
204 urations for which the velocity profile was considered as uniform, this hypothesis making  
205 it possible to consider the spatial variations of the pressure level alone. In the first con-  
206 figuration, the spatial distribution of the pressure level at a fixed depth was flat, whereas  
207 in the second (which seems more realistic) it was Gaussian.

#### 208 *Discrimination techniques*

209 By assuming that the URF sufficiently modifies the microbubble trajectory to be observed  
210 within the Doppler frequency, it seems natural to propose a discrimination technique  
211 based on the detection of Doppler frequency variations. Estimation of the frequency  
212 modulation index (FMI) seems to be highly appropriate to detect and quantify these  
213 additional accelerations. FMI can be defined by:

$$214 \quad FMI(t) = \frac{dF_D(t)}{dt}, \quad (16)$$

215 where  $F_D = 2fV_b \cos\theta/c$  is the Doppler frequency available from a time-frequency repre-  
216 sentation ( $V_b$  is the microbubble velocity). For instance with  $\theta = 5$  degrees,  $V = 0.5$  m/s,  
217  $f = 2$  MHz,  $c = 1500$  m/s,  $F_D = 950$  Hz. It was more convenient to evaluate the FMI  
218 from standard TCD recordings off-line, as real time calculation was too time-consuming  
219 for our experimental instrumentation.

220 Similarly, if a multi-gate TCD system is available (Guidi et al. (2003)), it is also possible  
221 to detect and quantify accelerations by means of the position modulation index (PMI).

222 For instance, PMI can be defined by:

$$223 \quad PMI(t) = \frac{dP_e(t)}{dt}, \quad (17)$$

224 where  $P_e$  is the microembolus position available from a time-depth representation (see  
225 Girault et al. (2010) for example). From evaluated FMI/PMI and by setting an empirical  
226 threshold, it is possible to detect and discriminate microemboli.

227 As the two proposed discrimination techniques are off-line techniques, no particular rec-  
228 ommendation are required during the TCD recording whatever the clinical scenario or  
229 the brain region explored.

230 To summarize, we present two models of the radiation force derived from the work of  
231 Doinikov (1998). These two models were incorporated into a numerical model which per-  
232 mits calculation of microembolus trajectories in the blood flow. Simulations highlighting  
233 the effects of these parameters on the trajectory of the microembolus are presented in the  
234 results section. Two parameters, i.e. FMI and PMI, are proposed to detect microembolus  
235 "additional acceleration".

## 236 **Results**

237 In this section we present the results obtained from simulations of the radiation force (see  
238 Figs. 2, 3, 4) and from simulations of the microembolus displacement (see Figs. 5, 6, 7 and  
239 Tables 2, 3). In order to validate the different models proposed, we compared simulated  
240 data to data derived from the literature (Smith et al., 1997), (Girault et al., 2010). The  
241 physical parameters used for these simulations are given in Table 1. Finally, though a  
242 microembolus can be a few hundred microns in size, we chose to limit the simulation size  
243 range to 1 – 100 microns because the proposed models are not valid beyond this range.

245 As the ultimate goal was the differentiation of gaseous and formed elements, initially the  
246 URFs acting on a microbubble and on a solid particle were compared. To understand  
247 fully the ways in which such forces differ, each loss involved in the calculation of the URF  
248 was evaluated. Furthermore, as in practice the sizes of microemboli are unknown, it is  
249 important to carry out simulations for various sizes.

250 We present first the simulations using the simplified Doinikov model (eqn. (4)) for a  
251 solid particle immersed in blood and then we present the simulations using the simplified  
252 Doinikov model (eqn. (5)) for a microbubble.

#### 253 *Ultrasound radiation force acting on a solid particle immersed in blood*

254 In this part of the study, the losses and then the radiation force were evaluated for various  
255 sizes. By comparing  $(kR_0)^3$  to  $\delta_v/R_0$  and  $\delta_t/R_0$  in eqn. (4), it was possible to evaluate  
256 which term would predominate at each  $R_0$  value. These three terms were compared for  
257 different frequencies (1, 2 and 3 MHz). The simulated results plotted in Fig.2 show that  
258 viscous and thermal effects in eqn. (4) predominated in an area of a few microns ( $30\mu m$ ).  
259 Above this value, the thermal and the viscous effects were insignificant. For radii of less  
260 than 10 microns, the losses (thermal and viscous) were higher for low frequencies than  
261 for high frequencies. This means that a high emitting frequency is better than a low  
262 frequency. For radii greater than 10 microns, the loss (mainly acoustic) was lower for low  
263 frequencies than for high frequencies. This means that a low emitting frequency is better  
264 than a high frequency. To ensure a good trade-off in terms of losses, the middle frequency  
265 ( $2 MHz$ ) was selected for the rest of the study.

266 In terms of the URF, the simulated results plotted in Fig.3 (obtained with a pressure  
267 level  $P = 500kPa$  and an emitting frequency  $f = 2MHz$ ) show that the URF acting on  
268 a solid particle was weak since its amplitude was below  $0.01\mu N$ . However, as the URF

269 increases with size, it is highly probable that for a quasi millimetric solid microembolus  
270 the URF is no longer negligible.

### 271 *Ultrasound radiation force acting on a gaseous microembolus immersed in blood*

272 In this part of the study, the losses and then the URF were evaluated for various sizes. In  
273 order to establish which effects predominated (acoustic, viscous, thermal), we simulated  
274 the weighted factor  $K$  (see eqn. (10)) and its three components  $K_0$ ,  $K_1$  and  $K_2$ . We also  
275 simulated the damping constants (see eqn. (7))  $\beta_{ac}$ ,  $\beta_{vis}$  and  $\beta_{th}$ . These simulations were  
276 performed for a fixed pressure level ( $P = 500\text{kPa}$ ), a fixed emitting frequency ( $f = 2\text{MHz}$ )  
277 and different radii ( $1 - 100\mu\text{m}$ ). Fig.4b shows that:

- 278 • thermal damping predominated for a radius  $< 2\mu\text{m}$ ;
- 279 • viscous damping predominated for  $2\mu\text{m} < R_0 < 5\mu\text{m}$ ;
- 280 • acoustic damping predominated for a radius  $> 5\mu\text{m}$ .

281 Fig.4a shows that for  $f = 2\text{MHz}$  the global factor  $K$  was substantially influenced by the  
282 terms attached to  $K_0$  (acoustic losses) and  $K_1$  (viscous losses) for  $2\mu\text{m} < R_0 < 30\mu\text{m}$ .

283 Fig.3 shows that the URF acting on a gaseous microembolus was far higher than that  
284 acting on a fat microembolus. Moreover, as depicted in this figure, the resonance angular  
285 frequency  $\omega'_0$  was slightly shifted from  $\omega_0$  (which corresponded to the resonance angular  
286 frequency in the case of a perfect fluid). Furthermore, due to dissipative effects, the  
287 resonance was spread more widely and thus less sharply than that obtained from an ideal  
288 fluid.

289 To summarize, we showed for both microbubbles and fat particles that the losses which  
290 limited the level of the URF were principally the thermal effects for radii of less than  
291 ten microns and acoustic effects for radii greater than ten microns. We also showed that  
292 URF acting on microbubbles were far higher than those acting on formed elements, thus  
293 leaving a question regarding microbubble displacement in comparison with that of a fat

294 particle.

### 295 *Displacement*

296 The main purpose of these simulations (see Fig.5, Table 2, Table 3 and Fig.6) was to  
297 propose some novel explanations of the FMS, particularly for the "V" (reversed or unre-  
298 versed) shape of the time-frequency Doppler microembolic signature. Further significant  
299 aims were:

- 300 • to provide an order of magnitude of displacements induced by the radiation force and  
301 of corresponding measurable parameters (FMI, PMI);
- 302 • to improve understanding of the parameters which impact on microembolus displace-  
303 ment and FMI/PMI;
- 304 • to show the feasibility of discriminating between fat and gaseous microemboli in plasma  
305 (or water) for a wide range of radii;
- 306 • to predict and provide an order of magnitude of the cumulative displacement  $\Delta_D$  of a  
307 microembolus circulating in blood or water;
- 308 • to verify whether the *in vitro* measurements reported in the literature are compatible  
309 with the simulated values of  $\Delta_D$ ,  $F_D$ ,  $FMI$  and  $PMI$ .

### 310 *Cumulative displacement*

311 The aim of this simulation (see Fig.5) was to improve understanding of the evolution  
312 of cumulative displacement for different microembolus sizes (gaseous or fat) and to pro-  
313 vide an order of magnitude of the displacement. The elementary displacement of the  
314 microbubble is an interesting indicator since it is the direct consequence of the radiation  
315 force. However, as its value is very low, calculation of the cumulative displacement is  
316 preferred.

317 Fig.5 shows that the cumulative displacements for both gaseous and formed elements

318 produced a shape relatively close to the shape of the corresponding URF. However, there  
319 were some small differences. It can be seen in Fig.3 that the URF level was the same for  
320 gaseous microemboli of 2 microns and 20 microns, while the cumulative displacements  
321 for the same radii were different. As for the URF, the cumulative displacement was far  
322 higher for microbubbles compared to fat particles.

323 Fig.5 shows that the cumulative displacements of gaseous microemboli were of a few  
324 hundred microns while those obtained for fat microemboli were of less than ten microns.  
325 Note that, as the cumulative displacement obtained for a fat microembolus was less  
326 than  $10 \mu m$  in the size range under consideration, only cumulative displacements of air  
327 microbubbles are considered below. Fig.5 shows that the higher the pressure level, the  
328 higher the cumulative displacement. This trend can also be seen in Table 3.

329 Fig.5 also shows that the mass effect, which is expressed as a force resisting the radiation  
330 force, has a significant effect on microembolus displacement. This mass effect is clearly  
331 described in equation 1 expressing Newton's law. For a fixed size, the microembolus  
332 displacement due to the radiation force will be greater for a microbubble (lightweight)  
333 than for a microparticle of fat (heavy): the heavier the microembolus the more difficult  
334 its displacement. It can thus be assumed that in practice for larger microbubbles and  
335 microparticles the microembolus displacement will be less for larger sizes.

### 336 *Measurable parameters*

337 Measurable parameters such as  $\Delta_D$ ,  $F_D(t)$ ,  $FMI(t)$ ,  $PMI(t)$  are presented in Table 2 for  
338 different pressure levels and in Table 3 for different velocity values.

339 As Table 2 shows, the lower the losses, the higher the maximum Doppler frequency, the  
340 higher the maximum of the frequency modulation index and the higher the maximum of  
341 the position modulation index.

342 As shown in Table 3, the higher the flow velocity, the lower the transit time, the lower

343 the number of pulses, and the lower the cumulative displacement. Indeed, the faster the  
344 blood flow, the less often the microbubble is pushed and the lower the cumulative effect.  
345 On the other hand, the higher the blood velocity, the higher the Doppler frequency, FMI  
346 and PMI. The radial and the longitudinal cumulative displacements were in the order of  
347 a few tens of microns and a few tens of millimeters, respectively.

348 Note also in Table 2 and Table 3 that FMI and PMI were in the order of a few kiloHertz  
349 and a few hundred millimeters, respectively.

### 350 *Acoustic beam and velocity profile*

351 Fig. 6 shows that the cumulative displacement, Doppler frequency, frequency modulation  
352 index and position modulation index were very different for different configurations (plug  
353 velocity-flat US beam, plug velocity-Gaussian US beam, laminar velocity-flat US beam,  
354 laminar velocity-flat US beam). This suggests that the spatial distribution of the velocity  
355 and the pressure level have important roles in the dynamics of displacement.

356 Maximum  $F_D$ ,  $PMI$  and  $FMI$  were obtained for plug and flat profiles.  $Max(FMI)$   
357 was about  $30\text{ kHz}$  for a gaseous microembolus of  $100\ \mu\text{m}$  radius whereas for a gaseous  
358 microembolus of  $2\ \mu\text{m}$  the  $max(FMI)$  reached  $100\text{ kHz/s}$ . The size of the microembolus  
359 impacted considerably on the  $FMI$ .

### 360 *Simulated FM signatures*

361 In order to prove definitively that the URF can explain all the FM signatures reported  
362 in the literature, a series of temporal and time-frequency representations of simulated  
363 Doppler MES is presented in Fig.7, similar to those obtained by Tortoli et al. (2000) for  
364 the three types of FM identified by Smith et al. (1997). The microembolus was located  
365 near the upper wall of the artery or near the center of the artery. The velocity profile was  
366 laminar, and the size of the microembolus was 100 microns.

367 Fig. 7a shows the temporal and time-frequency representations of a fat microembolus.  
368 As the radiation force was very weak, no frequency modulation was observed.

369 Fig.7c shows the temporal and time-frequency representations of a gaseous microembolus  
370 (a gradual modulation (type II) was observed) located near the upper wall of the artery  
371 for a low beam-to-flow angle and a laminar velocity profile. The predominant microdis-  
372 placement induced by the radiation force in these conditions was mainly longitudinal and  
373 involved no rapid changes in the spectral contents (force principally pushed in the flow  
374 direction) but rather a gradual increase or decrease. Note that when the beam-to-flow  
375 angle was smaller, the transit time was longer and the FMI (or PMI) lower but the mea-  
376 surement of the FMI was easier (or PMI). As Smith et al. (1997) reported that type II  
377 frequency modulations were also probably due to formed elements, we conjectured that  
378 solid microemboli greater than 100 microns could generate such an FMS.

379 Figs. 7b and 7d show the temporal and time-frequency representations of a gaseous  
380 microembolus located near the upper wall of the artery, a high beam-to-flow angle and a  
381 laminar velocity profile. In these conditions the predominant microdisplacement induced  
382 by the radiation force was mainly radial and involved rapid changes in the spectral content  
383 (the force principally pushed in the orthogonal direction of the blood flow). Note that  
384 the transit time was shorter and the FMI (or PMI) higher the greater the beam-to-flow  
385 angle but the measurement of the FMI (or PMI) was more difficult.

386 The gaseous microembolus in Fig.7d was located near the center of the artery, the angle  
387 was high and the velocity profile was laminar. In these conditions, the microbubble ac-  
388 celerated from the upper wall up to the center of the artery and decelerated to go outside  
389 the sample volume. The FM resembled an inverted "V" shape.

390 By comparing the FMI measured from the time-frequency domain of the simulated  
391 Doppler signal,  $FMI < 0.1$  kHz for a solid particle and  $FMI > 20$  kHz for a microbubble,  
392 we showed that it was possible to discriminate gaseous from solid microemboli.

393 To summarize, we showed that microdisplacements measured directly by PMI and indi-  
394 rectly by FMI are far greater for microbubbles than for formed elements. On the other  
395 hand, we established that the lower the acoustic losses, the higher the FMI and PMI. We  
396 also showed that the most important parameters which affected trajectory modification  
397 that could help to explain the variations in FMS were the spatial velocity distribution,  
398 the spatial pressure distribution, the beam-to-flow angle and the size of the microbubble.

## 399 **Discussion and Summary**

400 This section is divided into two parts, the first contains the discussion of the radiation  
401 force and the second the microdisplacements measured by FMI and PMI.

### 402 *Ultrasound radiation force*

403 As already demonstrated by Doinikov (1998) for a solid particulate in a non-perfect  
404 fluid, we showed that the radiation pressure exerted by the progressive plane wave was  
405 no longer proportional to  $(R_0^6 k^4)$ , as in the model presented by King (1934), but was  
406 proportional to  $(R_0^2 k)$ . Thus, even though they are small (see Fig.2), the viscous and  
407 thermal effects can cause substantial modifications and increased radiation pressure. Note  
408 that the predominating loss for radii smaller than ten microns originated from thermal  
409 phenomena whereas the predominating loss for radii greater than ten microns originated  
410 from acoustic phenomena, indicating that the best descriptive model is the Yosioka and  
411 Kawasima (1955) model.

412 The results illustrated in Fig.3 are very interesting because they show that the URF  
413 acting on a gaseous microembolus was far higher than that acting on a fat microembolus.  
414 This is explained by the fact that the sudden change in impedance between plasma and  
415 the air microbubble was greater than that between plasma and the piece of fat. This result  
416 was valid for radii less than  $100\mu\text{m}$ , whatever the model used. The results illustrated in

417 Fig.3 also show that the URF (Doinikov model) for microembolus sizes ranging from 10  
418 to 100 microns acting on a microbubble was always greater than that acting on a fat  
419 microembolus. These results are encouraging for the purpose of discrimination. Indeed,  
420 using only Doinikov's theory, it can be seen from the simulations plotted on Fig.3 that it is  
421 possible to discriminate between gaseous and fat microemboli ranging in radius between  
422  $1\mu\text{ m}$  and  $100\mu\text{ m}$  by setting a detection threshold at 10 nN, discriminating in practice  
423 between small gaseous microemboli (a few tens of microns) and large solid microemboli  
424 (a few hundred microns).

425 By comparing the different models presented, it can be seen that the asymptotic be-  
426 havior of the Yosioka and Kawasima (1955) model was similar to that of the Doinikov  
427 (1998) model for large radii while for small radii the Yosioka and Kawasima model un-  
428 derestimated the URF: this was due mainly to the thermal and viscous effects. More  
429 precisely, as illustrated in Fig.4, the viscous and thermal effects predominated for very  
430 small microbubbles compared to the acoustic damping, i.e. when  $(kR_0)^3 \ll \delta_v/R_0 \ll 1$   
431 and  $(kR_0)^3 \ll \delta_t/R_0 \ll 1$ . This was confirmed by the viscosity damping formula  
432  $(\beta_{vis} = \frac{2\eta}{\rho R_0^2})$  which is inversely proportional to the microbubble radius: the smaller the  
433 microbubble, the higher the viscous damping. It should also be noted that another conse-  
434 quence of the effects of thermal and viscous damping was that, apart from the resonance  
435  $\omega'_0$ , the radiation force given by eqn.(5) was greater than that obtained for a perfect fluid  
436 (i.e. the Yosioka and Kawasima model). This is in good agreement with the fact that  
437 damping effects reduce the amplitude of the radiation force at the resonance frequency.

438 Moreover, due to the surface tension, the resonance angular frequency  $\omega_0$  corresponding  
439 to the Yosioka and Kawasima model (surface tension not taken into account in this model)  
440 was slightly different from  $\omega'_0$  in the Doinikov model ( $\omega'_0 > \omega_0$ ).

441 By comparing the model proposed by Leighton (1994), it could be seen that the asymp-  
442 totic behaviors for both small and large radii were different from those of the Doinikov  
443 model. This was mainly due to the fact that the total damping term ( $\beta_{tot} = \delta_{tot}\omega'_0/2 =$

444  $0.1\omega'_0$ ) proposed by Leighton (1994) is different from the total damping term proposed  
 445 by Doinikov (1998) (eqn.(7)) and also to the fact that the resonance angular frequency  
 446  $\omega'_0 = \omega_0\sqrt{1+2K_3}$  proposed by Tortoli et al. (2000) is slightly different from the reso-  
 447 nance angular frequency  $\omega'_0 = \omega_0\sqrt{1-K_3}$  proposed by Doinikov (1998). The resonance  
 448 angular frequency presented by Tortoli et al. (2000) was between  $\omega_0$  and the  $\omega'_0$  defined  
 449 by Doinikov (1998).

450 Note that, three theoretical models of the URF acting on a single microbubble can be  
 451 recognized with different values of  $K$ ,  $K_2$  and  $K_3$  (see below):

- 452 • the Doinikov model (eqn. (5)) where  $K_2 = 1 - K_3$  with  $K_3 = \frac{2\tilde{\sigma}}{3R_0\rho c^2}$ ;
- 453 • the Yosioka and Kawasima (1955) model for (eqn. (5)) where  $\beta_{vis} = \beta_{th} = 0$ ,  $K = 1$ ,  
 454  $K_3 = 0$  and  $K_2 = 1$ ;
- 455 • the Leighton (1994) (p.343), and Dayton et al. (1997) models, (where  $K = 1$  in eqn.  
 456 (5)), and Tortoli et al. (2000)'s model (where  $K = 1$ ,  $K_2 = 1 + 2K_3$  and  $2\beta_{tot} = \delta_{tot}\omega_0$   
 457 in eqn. (5). The  $\delta_{tot}$  for a microbubble of 2 microns radius obtained at resonance  
 458 frequency in water ( $f'_0 = 1.83\text{MHz}$ ) is equal to 0.2 (see Leighton (1994)). The latter  
 459 model provides a radiation force which is almost always greater than that provided by  
 460 the Doinikov model. Note also that the resonance angular frequency is between  $\omega'_0$  and  
 461  $\omega_0$ .

462 In summary, the URF acting on a microbubble is very different from that acting on a fat  
 463 particle both in terms of levels and in terms of trends whatever the model. More precisely,  
 464 whatever the size range studied, the URF acting on a microbubble is far higher than that  
 465 acting on a fat particle, which is an important point for discrimination purposes.

#### 466 *Displacement*

467 We discuss here the cumulative displacement of a microbubble, the measurable param-  
 468 eters, parameters which impact on the microembolus trajectory and the different FM

469 signatures observed in practice.

#### 470 *Cumulative displacement*

471 The displacement analysis showed that :

- 472 • the cumulative displacement of gaseous microemboli (a few hundred microns) was  
473 greater than those obtained for fat microemboli (less than ten microns). This deviation  
474 by a factor of ten corroborates the above results concerning the radiation force, and is  
475 encouraging for discrimination purposes;
- 476 • for roughly similar conditions the simulated microbubble displacement (a few hundred  
477 microns) was similar to that measured by Palanchon et al. (2005), indicating that the  
478 models proposed by Leighton (1994) and adapted by Tortoli et al. (2000) and Doinikov  
479 (1996) were good models and probably appropriate;
- 480 • the cumulative displacement increased with the pressure level, explained in part by the  
481 fact that the URF was proportional to the pressure level  $P$ .
- 482 • the evolution of the cumulative displacement in relation to microembolus size followed  
483 the same trends as the radiation force. These results were consistent. However, there  
484 were some small differences, mainly explained by the fact that the mass effect was  
485 greater for high microembolus sizes, suggesting that as size increases the displacement  
486 decreases. This seems to demonstrate that the signature will be large and the dis-  
487 placement will be small for large fat particles, whereas both the signature and the  
488 displacement will be large for large bubbles. This hypothesis remains to be confirmed.

#### 489 *Measurable parameters*

490 It is interesting that all parameter values (summarized in Table 2) were higher for higher  
491 pressure levels, except for the transit time and the number of pulses. This phenomenon is  
492 readily explained by the fact that the radiation force was stronger and the microembolus  
493 velocity was higher when the acoustic pressure was greater (or the displacement per time

494 unit). Since the Doppler frequency was proportional to the microembolus velocity, the  
495 higher the velocity the higher the Doppler frequency. The same applied for  $FMI$  and  
496  $PMI$ . Lastly, both the time spent by the microembolus in the sample volume and the  
497 number of pulses were reduced by increasing the velocity.

498 It should be noted that, although the reported displacements were small, they were non-  
499 negligible with regard to a TCD system. Indeed, by assuming a typical system with 8kHz  
500 PRF and 128 point FFT (the time resolution being  $128/8000=16$  ms and the spectral res-  
501 olution  $8000/128=62.5$ Hz), the lowest detectable FMI would be  $62.5\text{Hz}/16\text{ms}=3.9\text{kHz/s}$ .  
502 This implies that the lowest detectable  $FMI$  corresponds to losses below 10 dB, which  
503 seems to correspond to patients with a narrow temporal window. If we consider that the  
504 radiation force is indeed the phenomenon which underlies the presence of a high FMI or  
505 the presence of a "V" shaped time-frequency, it would be logical to suggest that these  
506 phenomena would be observed only in patients with a narrow temporal window.

507 Moreover, comparing the simulated values to the practical values reported by (Girault  
508 et al., 2010) showed that, though the experiment slightly differed from the simulation,  
509 the differences between them were small. For example, comparing  $FMI$  values extracted  
510 from Table 3 for 150 kPa ( $0.23 < \max(FMI) < 2.04$  kHz/s) with the measured  $FMI$   
511 extracted from Fig.10 in (Girault et al., 2010) with a skull ( $0.16 < \max(FMI) < 2$   
512 kHz/s) and  $FMI$  values extracted from Table 3 for 500 kPa ( $3.52 < \max(FMI) < 19.46$   
513 kHz/s) with the measured  $FMI$  extracted from Fig.10 in (Girault et al., 2010) without a  
514 skull ( $4 < FMI < 40$  kHz/s), it was obvious that these values were of the same order, in  
515 part validating the simulation models. We attributed the discrepancy to the fact that the  
516 surrounding medium was different (blood/water) and also to the fact that parameters such  
517 as microembolus size, fluid velocity, temperature, etc, had not been clearly established  
518 or were not known.

519 To summarize, it is easier to execute practical measurements when the pressure level is  
520 high than when the duration of the Doppler signal is low. Furthermore, the thinner the

521 temporal bone the easier it is to execute the measurements. Moreover, though conditions  
522 differed slightly, the practical values reported in the literature are similar to our simulated  
523 values.

#### 524 *Acoustic beam and velocity profile*

525 The findings extracted from Fig.6 show clearly that the spatial distributions of both  
526 velocity and pressure have important roles in terms of shape and values. The spatial  
527 distribution of pressure has a marked role in the shape of the FMS rather than in terms  
528 of the Doppler frequency value. In contrast, the spatial distribution of velocity has a  
529 marked role in terms of Doppler frequency value rather than in the shape of the FMS. In  
530 the case of a pulsatile flow, the shape and the value of the additional acceleration seems  
531 to be very complex and unpredictable. Note also that the size of the microbubble seems  
532 to be another parameter which affects the microbubble trajectory.

#### 533 *Simulated FM signatures*

534 Finally, the results illustrated in Fig.7 show considerable similarities between the *in vivo*  
535 and *in vitro* experiments reported in the literature (Smith et al. (1997), Girault et al.  
536 (2010)) and in our simulations, seeming to confirm that our models are very applicable  
537 to this situation.

538 We also showed that by setting a constant threshold of 1 kHz/s it was possible to dif-  
539 ferentiate between microbubbles and solid particles from FMI evaluated from simulated  
540 Doppler signals, confirming previously published results (Smith et al. (1997)).

541 We showed that the beam-to-flow angle, the type and size of the microembolus, the  
542 spatial distribution of the velocity and the pressure level all have non-negligible roles in  
543 the FMS, demonstrating that it is possible to explain all FMS for the following reasons:

- 544 • For "type I" the radiation is not enough to push the solid particle, and therefore no  
545 FM is present. The microembolus circulates at the same velocity as blood;
- 546 • For "type II", involving microbubbles and large micro-particles, the UFR acts in the  
547 same direction as the blood flow and thus microemboli are accelerated gradually;
- 548 • For "type III" involving only microbubbles:
- 549 (1) The first explanation is based on the fact that it is necessary to take into account the  
550 pulsatility of flow. Thus, on the basis that the blood flow is time-varying, and that  
551 outside the sample volume the microbubble is near the center of the artery during  
552 the diastole phase, at this instant in time the microbubble velocity is quasi maximal.  
553 When the microbubble enters the sample volume, it moves towards the wall due to  
554 the radiation force, and the microbubble decelerates. A few milliseconds later, the  
555 microbubble enters the systole phase with the same flow-line as in the diastole phase.  
556 The microbubble then accelerates, since the maximum value of the flow accelerates.  
557 As the microbubble is pushed towards the artery wall, the microbubble slows down.  
558 The form of the FM thus drawn resembles a "V".
- 559 (2) For the last explanation, instead of focusing on the velocity profile, it is also possible  
560 to explain the "V" shape or the inverted "V" shape by taking into account only the  
561 spatial variations present in the ultrasound field. By assuming a plug velocity profile  
562 (ensuring no spatial variations in the blood velocity), if the US beam is located in  
563 such a way that the principal lobe of the US beam in the sample volume is located  
564 near the upper wall and the second lobe is located near the lower wall, then the  
565 pressure level in the center of the artery is very low. A "V" shape is then visualized  
566 on the TCD for this configuration since the high displacements are near the walls  
567 whereas low displacements are in the center. It can be seen that it is possible to  
568 image most of the unusual and varied FMS by combining both the velocity and the  
569 US beam profiles.

570 However, it should be noted that detection of a Type III FMS rules out solid emboli and  
571 therefore the physician will understand that no dramatic action is required. Detection

572 of a non-Type III FMS does not characterize a solid or a gas, because we do not know  
573 about emboli  $> 100$  microns. Further studies are therefore required to provide information  
574 regarding the significance of non-Type III FMS signals for physicians.

575 To summarize, two analytical models of the URF and a numerical model of displace-  
576 ment are proposed. Simulation results, which were in a good agreement with experiments  
577 reported in the literature, validated the numerical models, thus confirming that the ra-  
578 diation force should no longer be ignored in the process generating the various shapes of  
579 the FM signatures.

580 The most important parameters which affect and therefore explain most FMS encountered  
581 in practice are the spatial distributions of velocity and pressure, the pulsatility of the  
582 blood flow, microbubble size and the beam-to-flow angle. Several valid hypotheses are  
583 proposed to explain the different types of FMS. Finally, our study confirms that FMI (and  
584 PMI) provide valuable information on which discrimination techniques can be based.

## 585 **Acknowledgements**

586 This study was supported by the European Union (UMEDS Project) and by the French  
587 Government (CASC Project). We wish to thank P. Tortoli for valuable discussions.

## 588 **References**

- 589 Asaki, T. J., Marston, P., 1994. Acoustic radiation force on a bubble driven above reso-  
590 nance. *J. Acoust. Soc. Am*, 3096–3099.
- 591 Benocci, C., Buchlin, J.-M., Michelassi, V., Weinacht, P., 1986. Numerical modelling of  
592 gas-droplet flows for industrial applications. presented at the 3rd Int. Con. Computa-  
593 tional Methods Expe. Measure., Porto Carras, Greece,.

594 Cowe, J., Grittins, J., Naylor, A., Evans, D., 2002. Rf signals provide additional informa-  
595 tion on embolic events recorded during tcd monitoring. *Ultrasound in medicine and*  
596 *biology* 31, 613–623.

597 Dayton, P. A., Morgan, K. E., Klibanov, A. L., Brandenburger, G., Nightingale, K. R.,  
598 Ferrara, K. W., 1997. A preliminary evaluation of the effects of primary and secondary  
599 radiation forces on acoustic contrast agents. *IEEE Trans. Ultrason., Ferroelect., Freq.*  
600 *Contr.* 44, 1264–1277.

601 Devuyst, G., Darbellay, G., Vesin, J.-M., Kemeny, V., Ritter, M., Droste, D., Moline,  
602 C., Serena, J., Sztajzel, R., Ruchat, P., and G. Dietler, C. L., Ringelstein, E., 2001.  
603 Automatic classification of hits into artifacts or solid or gaseous emboli by a wavelet  
604 representation combined with dual gated tcd. *Ultrasound in medicine and biology* 27,  
605 2803–2809.

606 Devuyst, G., Vesin, J.-M., Despland, P.-A., Bogousslavsky, J., 2000. The matching pursuit  
607 method: a new method of characterizing micro-emboli signals ? *Ultrasound in medicine*  
608 *and biology* 26, 1051–1056.

609 Doinikov, A., 1996. On the radiation pressure on a small spheres. *J. Acoust. Soc. Am.*  
610 100, 1231–1233.

611 Doinikov, A., 1997a. Acoustic radiation force on a spherical particle in a viscous heat-  
612 conducting fluid. i. general formula. *J. Acoust. Soc. Am.* 101, 713–721.

613 Doinikov, A., 1997b. Acoustic radiation force on a spherical particle in a viscous heat-  
614 conducting fluid. ii. force on a rigid sphere. *J. Acoust. Soc. Am.* 101, 722–730.

615 Doinikov, A., 1997c. Acoustic radiation force on a spherical particle in a viscous heat-  
616 conducting fluid. iii. force on a liquid drop. *J. Acoust. Soc. Am.* 101, 731–740.

617 Doinikov, A., 1998. Acoustic radiation force on bubble: viscous and thermal effect. *J.*  
618 *Acoust. Soc. Am.* 103, 143–147.

619 Georgiadis, D., Mackay, T., Kelman, A., Grosset, D., Wheatley, D., Lees, D., 1994. Dif-  
620 ferentiation between gaseous and formed embolic materials in vivo. application in pros-  
621 thetic heart valve patients. *Stroke* 25, 1559–1563.

622 Girault, J.-M., Kouame, D., Guidi, F., Menigot, S., Souchon, G., Tranquart, F., 2010.

623 Embolus discrimination by means of ultrasound radiation force part ii: Analysis of the  
624 frequency modulation by means of in vitro experiments. *Ultrasound in medicine and*  
625 *biology* XX, XX–XX.

626 Guidi, F., Boni, E., Tortoli, P., 2003. Acoustic method for real-time visualization of  
627 microbubble movements and rupture. *IEEE Ultrasonics symposium*, 1183–1186.

628 King, L., 1934. On the acoustic radiation pressure on spheres. *Proc. Roy. Soc. A.* 147,  
629 212–240.

630 Leighton, T. G., 1994. *The acoustic bubble*. New York: AcademicPress.

631 Markus, H., Brown, M., 1993. Differentiation between different pathological cerebral em-  
632 bolic materials using transcranial doppler in a in vitro model. *Stroke* 24, 1–5.

633 Mess, W., Willigiers, J., Ledoux, L., Ackerstaff, R., Hoeks, A., 2002. Microembolic sig-  
634 nal description: a reappraisal based on a customized digital postprocessing system.  
635 *Ultrasound in medicine and biology* 28, 1147–1455.

636 Palanchon, P., Tortoli, P., Bouakaz, A., Versluis, M., DeJong, N., 2005. Optical observa-  
637 tion of acoustical radiation force effects on individual air bubbles. *IEEE Trans. Ultra-*  
638 *son., Ferroelect., Freq. Contr.*, 104–110.

639 Prosperetti, A., 1977. Thermal effects and damping mechanisms in the forced radial  
640 oscillations of gas bubbles in liquids. *J. Acoust. Soc. Am.*, 17–27.

641 Rusell, D., Brucher, R., 2002. Online automatic discrimination between solid and gaseous  
642 cerebral microemboli with the first multifrequency transcranial doppler. *Stroke* 33,  
643 1975–1980.

644 Rusell, D., Madden, K., Clark, W., Sanset, P., Zivin, J., 1991. Detection of arterial emboli  
645 using doppler ultrasound in rabbits. *Stroke* 22, 253–258.

646 Smith, J., Evans, D., Bell, P., Naylor, R., 1998. A comparison of four methods for distin-  
647 guishing doppler signals from gaseous and particulate emboli. *Ultrasound in medicine*  
648 *and biology* 29, 1133–1138.

649 Smith, J., Evans, D., Naylor, R., 1997. Analysis of the frequency modulation present  
650 in doppler ultrasound signal may allow differentiation between partiulate and gaseous  
651 cerebral emboli. *Ultrasound in medicine and biology* 23, 727–734.

- 652 Souchon, G., Girault, J.-M., Biard, M., Kouamé, D., Tranquart, F., 2005. Gaseous and  
653 solid emboli differentiation using radiation force. IEEE Ultrasonics symposium, Rot-  
654 terdam, 2070–2073.
- 655 Tortoli, P., Pratesi, M., Michelasi, V., 2000. Doppler spectra from contrast agents crossing  
656 an ultrasound field. IEEE Trans. Ultrason., Ferroelect., Freq. Contr. 47, 716–725.
- 657 Yosioka, K., Kawasima, Y., 1955. Acoustic radiation pressure on a compressible sphere.  
658 Acustica 5, 167–173.

659 **List of Tables**

660	1	<b>Physical parameters</b>	34
661	2	<b><math>F_D</math>, <math>FMI</math> and <math>PMI</math> for a gaseous microembolus circulating in plasma, <math>I_{spta} = 720\text{mW}/\text{cm}^2</math>, <math>PRF = 8\text{kHz}</math>, <math>N = 40</math>, <math>L = 23\text{mm}</math>, <math>V = 1\text{m/s}</math>, <math>\theta = 5</math> degrees, <math>R_0 = 100 \mu\text{m}</math>, uniform (Plug) or laminar velocity profiles and uniform (Flat) or Gaussian US beam profiles.</b>	35
662			
663			
664			
665			
666	3	<b>Maximum FMI and maximum PMI for gaseous microemboli (100 <math>\mu\text{m}</math>) circulating in plasma (<math>\eta = 4\text{mPa.s}</math>), <math>PRF = 8\text{kHz}</math>, <math>f = 2\text{MHz}</math>, <math>N = 40</math>, <math>L = 23 \text{ mm}</math>, <math>\theta = 5</math> degrees for a laminar velocity profile and for a gaussian US beam. We assumed a gaseous microembolus with a radius of <math>R_0 = 100 \mu\text{m}</math> circulating in blood at a maximum velocity of <math>V = 0.5 \text{ m/s}</math> in an artery of 5 mm. The initial position of the microembolus in the artery was 4.5 mm.</b>	36
667			
668			
669			
670			
671			
672			

673 **List of Figures**

- 674 1 Forces acting on a microembolus in a fluid flow. 34
- 675 2  $k^3 R_0^3$ ,  $\delta_v/R_0$ ,  $\delta_t/R_0$  weighting factors for a fat microembolus embedded in  
676 blood. Viscous and thermal effects in relation to radius. These combined  
677 effects (viscous and thermal) predominated for microemboli below 30  $\mu\text{m}$ .  
678 The pressure level was set at  $P = 500$  kPa. 37
- 679 3 Discrimination between gaseous and solid microemboli circulating in  
680 plasma ( $\eta = 4$  mPa.s) using simplified Doinikov (1996), Doinikov (1998),  
681 Yosioka and Kawasima (1955) and Dayton et al. (1997) models. These  
682 curves show that viscous and thermal effects predominate below 30  $\mu\text{m}$ .  
683 Above 30  $\mu\text{m}$  the simplified Doinikov (1998) model was similar to the  
684 Yosioka and Kawasima (1955) model. Note that the model proposed by  
685 Dayton et al. (1997) did not give the same asymptotic value for high  
686 frequencies. Note also that the radiation force acting on a microbubble of  
687 2  $\mu\text{m}$  is equivalent to that acting on a microbubble of 20  $\mu\text{m}$ . 38
- 688 4 Weighting factors of eqn.(10) and damping coefficients of eqn.(7) for a  
689 gaseous microembolus immersed in blood. Viscous and thermal effects in  
690 relation to radius. These combined effects predominated for microemboli  
691 below 30  $\mu\text{m}$ . 39

- 692 5 Cumulative displacement  $\Delta_D^*$  of a gaseous microembolus in blood  
693 ( $\eta = 4\text{mPa}\cdot\text{s}$ ). Microembolus diameters ranged from  $1\mu\text{m}$  to  $100\mu\text{m}$   
694 (in order to verify the validity of the physical model).  $PRF = 8\text{kHz}$   
695 (commonly used PRF are 1, 5, 6, 8, 10 kHz),  $Pa = 500 - 150\text{ kPa}$ ,  
696  $f = 2\text{ MHz}$ ,  $V = 0.1\text{ m/s}$ ,  $N = 20$ , laminar profile, gaussian US beam,  
697 simplified Doinikov model. The duration of the pulse train was  $10\mu\text{s}$   
698 ( $4\mu\text{m}$ , (Mess et al., 2002)  $< 10\mu\text{m} < 13\mu\text{m}$  (Cowe et al., 2002)). The  
699 microembolus immersed in blood moved in a section of artery of 5 mm  
700 and the insonification angle was 5 degrees. Note that the US beam width  
701 revealing the microembolus was:  $L = 23\text{ mm}$ . The physical parameters  
702 for the medium studied are shown in Table 1. The initial position of the  
703 microembolus was set at 4.5 mm, *i.e.* near the upper wall of the tube (5  
704 mm). The microemboli were spherical. 40
- 705 6 Cumulative displacement, Doppler frequency, FMI and PMI for different  
706 fluid velocities in the case of a gaseous microembolus ( $R_0 = 100\ \mu\text{ m}$ )  
707 circulating in plasma.  $V = 0.5\text{ m/s}$ ,  $L = 23\text{ mm}$ ,  $PRF = 8\text{ kHz}$ ,  $f = 2$   
708 MHz,  $N = 20$ ,  $P = 500\text{ kPa}$ . 41
- 709 7 Time frequency representation of a simulated microembolic Doppler  
710 signal. a) As  $FMI < 0.1\text{kHz}$ , we concluded that there was no FM  
711 modulation (fat particle). c) Gradual modulation observed over most of  
712 the signal duration (microbubble near the upper artery wall),  $FMI > 20$   
713 kHz. b) Rapid change (reversed "V" shape) in the FM on a small  
714 percentage of the signal duration (microbubble near the artery center).  
715 The reversed "V" shape, which seems to be representative of a gaseous  
716 microembolic signature, is similar to that reported by Smith et al. (1997)  
717 and Girault et al. (2010). d) Rapid change in the FM on a small percentage  
718 of the signal duration (microbubble near the upper artery wall). FMI  
719 evaluated in the accelerating phase was  $\Delta_f/\Delta_t = 500/0.016 = 31\text{kHz/s}$ . 42

Table 1

**Physical parameters**

parameters/medium	host fluid		microembolus( $\sim$ )	
	water	plasma	fat	air
$\rho$ - density ( $kg/m^3$ )	1000	1055	952	1.1
$c$ -speed of sound ( $m/s$ )	1480	1580	1450	353
$\eta$ - viscosity (mPa.s)	1	4	40	0.018
$\chi$ - thermal diffusivity ( $\mu m^2/s$ )	0.10	0.11	0.20	28
$\kappa$ - thermal conductivity (J/smK)	0.58	-	-	0.034
$\nu$ - specific heat ratio	1	-	-	1.4

Note that the superficial tension of the air microbubble was  $\tilde{\sigma} = 72.10^{-3} N/m$  and

$$\tilde{p}_0 = 100kPa.$$

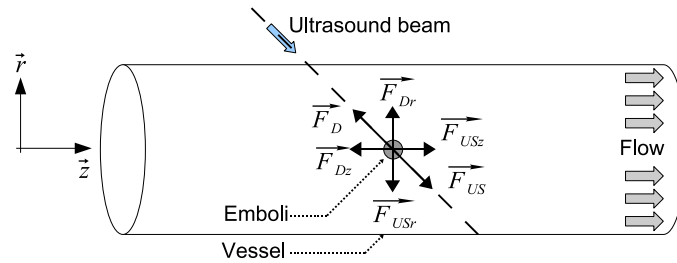


Fig. 1. Forces acting on a microembolus in a fluid flow.

Table 2

$F_D$ ,  $FMI$  and  $PMI$  for a gaseous microembolus circulating in plasma,  $I_{spta} = 720\text{mW/cm}^2$ ,  $PRF = 8\text{kHz}$ ,  $N = 40$ ,  $L = 23\text{mm}$ ,  $V = 1\text{m/s}$ ,  $\theta = 5$  degrees,  $R_0 = 100 \mu\text{m}$ , uniform (Plug) or laminar velocity profiles and uniform (Flat) or Gaussian US beam profiles.

Profiles	Plug, Flat					Laminar, Gaussian				
$loss$ (dB)	20	15	10	5	0	20	15	10	5	0
$P$ (kPa)	38	67	120	210	380	38	67	120	210	380
$max(F_D)$ (kHz)	1.87	1.88	1.89	1.91	1.95	0.68	0.68	0.69	0.71	0.76
$max(FMI)$ (kHz/s)	0.62	1.92	5.84	16.8	43.2	0.14	0.43	1.32	4.00	11.32
$max(PMI)$ (mm/s)	981	982	984	993	1015	353	353	355	360	378

To take into account the fact that the pressure level in the brain varies according to the patient, several levels of loss were simulated (0, 5, 10, 15, 20 dB). Different pressure values are proposed to cover the situations most commonly encountered in practice, corresponding to different types of loss such as reflections, diffraction effects and attenuation. To predict the losses encountered in *in vivo* conditions, the brain attenuation must be taken into account (attenuation coefficient 0.5 dB/cm/MHz). In this case the corresponding loss at 5 cm for an emitting frequency of 2 MHz would be 5 dB ( $0.5 \times 5 \times 2$ ), and the total loss would be 15 dB.

Table 3

**Maximum FMI and maximum PMI for gaseous microemboli ( $100 \mu\text{ m}$ ) circulating in plasma ( $\eta = 4\text{mPa}\cdot\text{s}$ ),  $PRF = 8\text{kHz}$ ,  $f = 2\text{MHz}$ ,  $N = 40$ ,  $L = 23 \text{ mm}$ ,  $\theta = 5 \text{ degrees}$  for a laminar velocity profile and for a gaussian US beam.** We assumed a gaseous microembolus with a radius of  $R_0 = 100 \mu\text{m}$  circulating in blood at a maximum velocity of  $V = 0.5 \text{ m/s}$  in an artery of  $5 \text{ mm}$ . The initial position of the microembolus in the artery was  $4.5 \text{ mm}$ .

$P(\text{kPa})$	150				500			
$V_{max} \text{ (m/s)}$	0.1	0.5	0.8	1	0.1	0.5	0.8	1
$\Delta_D^*(\text{mm})$	22.94	22.95	22.96	22.98	22.95	22.96	22.97	22.98
$\Delta_r(\text{mm})$	0.05	0.01	0.007	0.005	0.27	0.09	0.07	0.05
$\Delta_z^*(\text{mm})$	22.94	22.95	22.96	22.98	22.95	22.96	22.97	22.98
$max(FMI) \text{ (kHz/s)}$	0.23	1.05	1.65	2.04	3.52	10.76	16.02	19.46
$max(PMI) \text{ (mm/s)}$	41	180	286	356	93	233	335	403
$t_t \text{ (ms)}$	596	126	79	63	470	113	73	59
$N_{pulse}$	1887	1004	631	506	1358	900	588	477

If the blood is replaced by water, then for  $P = 500 \text{ kPa}$ ,  $V_{max} = 0.1 \text{ m/s}$ , and thus the cumulative displacement is  $\Delta_D^* = 22.95 \text{ mm}$ ,  $\Delta_r = 0.52 \text{ mm}$ ,  $max(FMI) = 13.2 \text{ kHz/s}$ ,  $max(PMI) = 170 \text{ mm/s}$ ,  $t_t = 394 \text{ ms}$  and  $N_{pulse} = 3150$ . These values are of the same order as those obtained for blood, and because the viscosity is lower, the microbubble crosses the sample volume more easily and thus more quickly. Note that for other values of  $PRF$  (1, 5, 6 kHz) and  $N$  (8, 10, 20, 30, 40), the simulation results were very close.

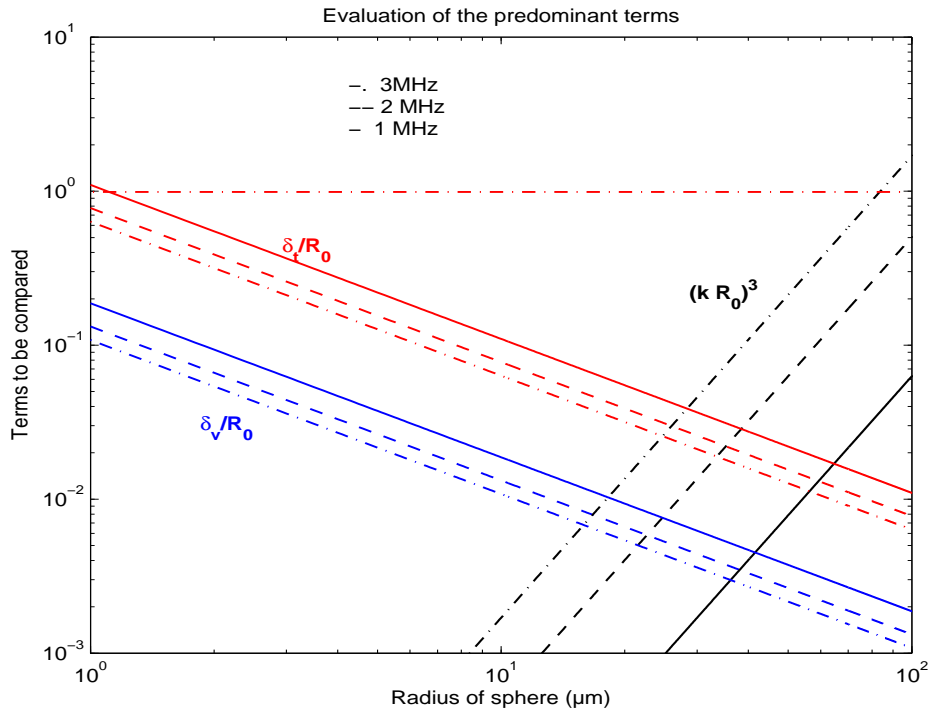


Fig. 2.  $k^3 R_0^3$ ,  $\delta_v/R_0$ ,  $\delta_t/R_0$  weighting factors for a fat microembolus embedded in blood. Viscous and thermal effects in relation to radius. These combined effects (viscous and thermal) predominated for microemboli below  $30 \mu\text{m}$ . The pressure level was set at  $P = 500 \text{ kPa}$ .

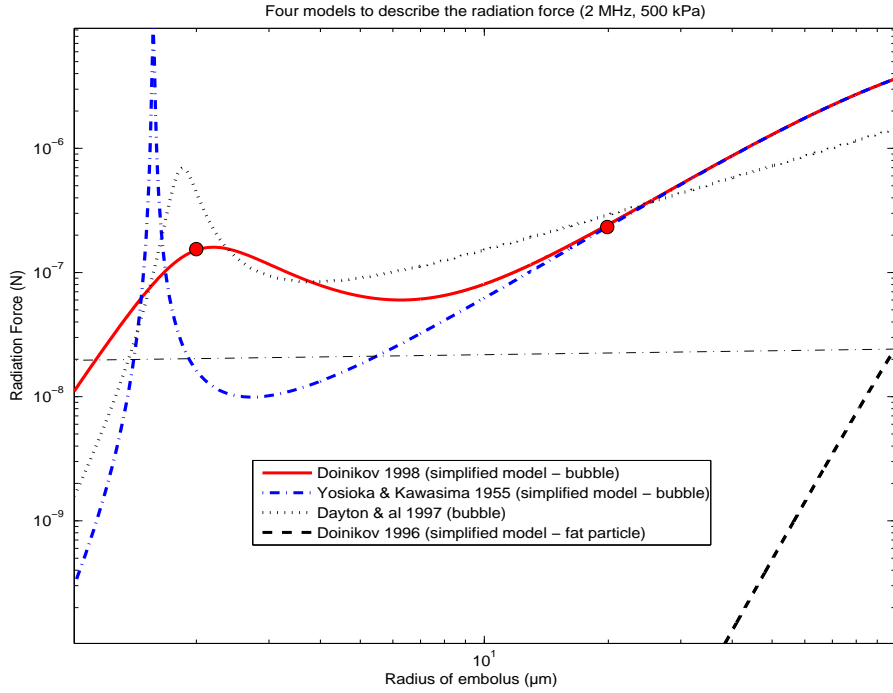


Fig. 3. Discrimination between gaseous and solid microemboli circulating in plasma ( $\eta = 4$  mPa.s) using simplified Doinikov (1996), Doinikov (1998), Yosioka and Kawasima (1955) and Dayton et al. (1997) models. These curves show that viscous and thermal effects predominate below  $30 \mu\text{m}$ . Above  $30 \mu\text{m}$  the simplified Doinikov (1998) model was similar to the Yosioka and Kawasima (1955) model. Note that the model proposed by Dayton et al. (1997) did not give the same asymptotic value for high frequencies. Note also that the radiation force acting on a microbubble of  $2 \mu\text{m}$  is equivalent to that acting on a microbubble of  $20 \mu\text{m}$ .

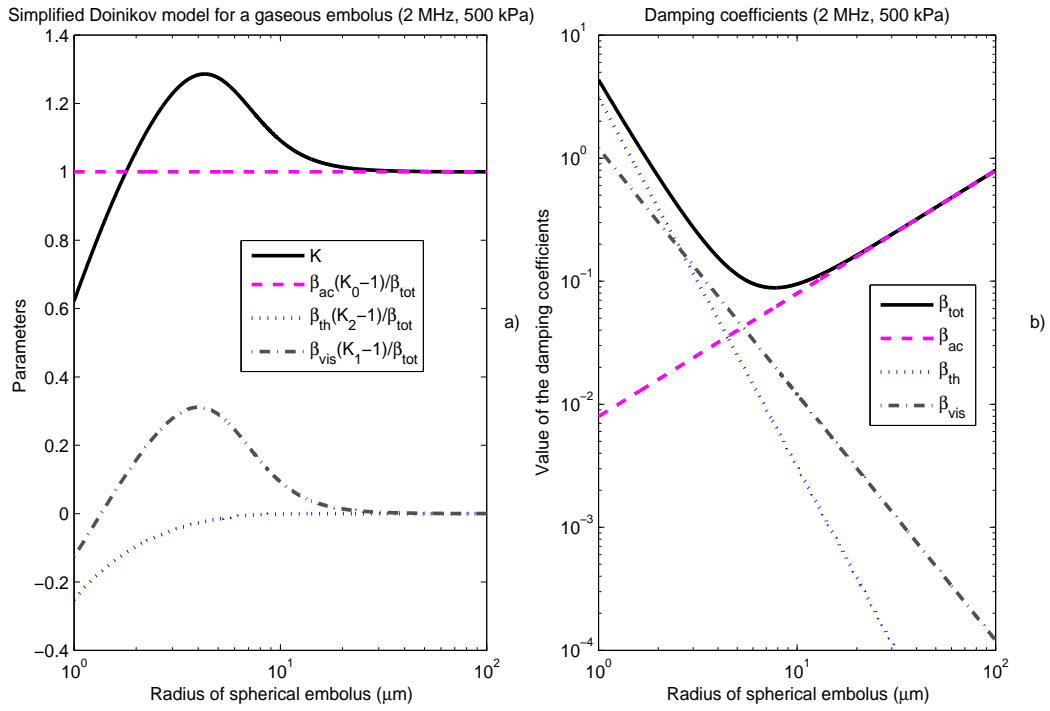


Fig. 4. Weighting factors of eqn.(10) and damping coefficients of eqn.(7) for a gaseous microembolus immersed in blood. Viscous and thermal effects in relation to radius. These combined effects predominated for microemboli below  $30 \mu\text{m}$ .

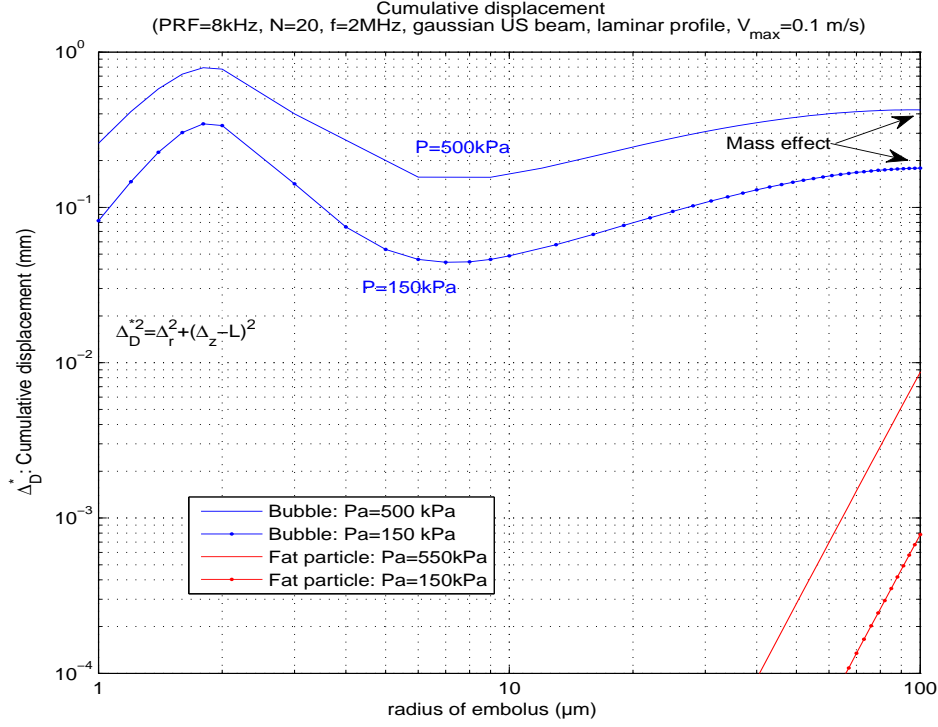


Fig. 5. Cumulative displacement  $\Delta_D^*$  of a gaseous microembolus in blood ( $\eta = 4\text{mPa}\cdot\text{s}$ ). Microembolus diameters ranged from  $1\mu\text{m}$  to  $100\mu\text{m}$  (in order to verify the validity of the physical model).  $PRF = 8\text{kHz}$  (commonly used PRF are 1, 5, 6, 8, 10 kHz),  $Pa = 500 - 150$  kPa,  $f = 2$  MHz,  $V = 0.1$  m/s,  $N = 20$ , laminar profile, gaussian US beam, simplified Doinikov model. The duration of the pulse train was  $10\mu\text{s}$  ( $4\mu\text{m}$ , (Mess et al., 2002)  $< 10\mu\text{m} < 13\mu\text{m}$  (Cowe et al., 2002)). The microembolus immersed in blood moved in a section of artery of 5 mm and the insonification angle was 5 degrees. Note that the US beam width revealing the microembolus was:  $L = 23$  mm. The physical parameters for the medium studied are shown in Table 1. The initial position of the microembolus was set at 4.5 mm, *i.e.* near the upper wall of the tube (5 mm). The microemboli were spherical.

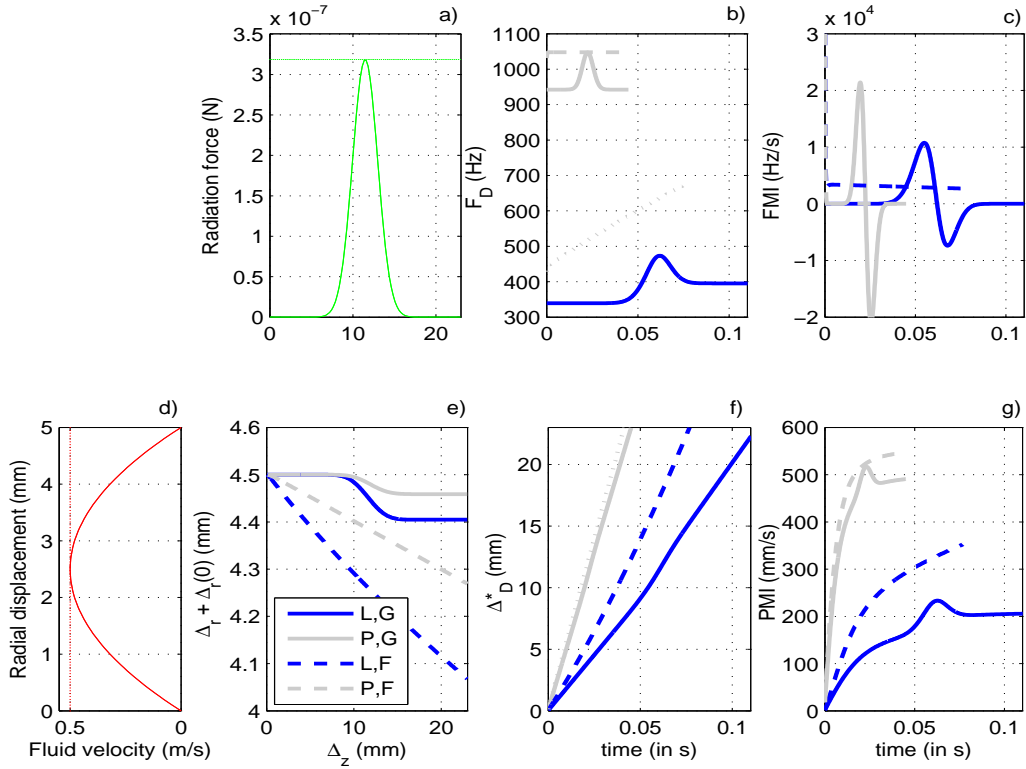


Fig. 6. Cumulative displacement, Doppler frequency, FMI and PMI for different fluid velocities in the case of a gaseous microembolus ( $R_0 = 100 \mu\text{m}$ ) circulating in plasma.  $V = 0.5 \text{ m/s}$ ,  $L = 23 \text{ mm}$ ,  $PRF = 8 \text{ kHz}$ ,  $f = 2 \text{ MHz}$ ,  $N = 20$ ,  $P = 500 \text{ kPa}$ .

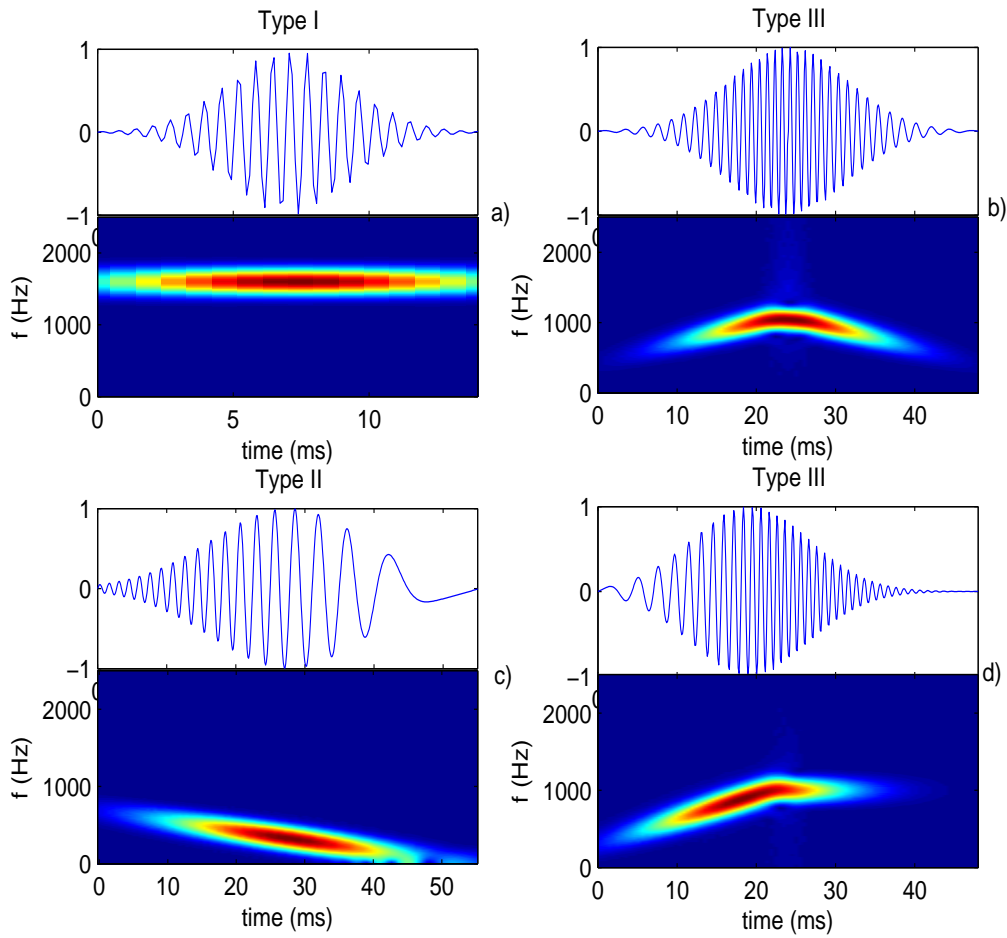


Fig. 7. Time frequency representation of a simulated microembolic Doppler signal. a) As  $FMI < 0.1\text{kHz}$ , we concluded that there was no FM modulation (fat particle). c) Gradual modulation observed over most of the signal duration (microbubble near the upper artery wall),  $FMI > 20\text{ kHz}$ . b) Rapid change (reversed "V" shape) in the FM on a small percentage of the signal duration (microbubble near the artery center). The reversed "V" shape, which seems to be representative of a gaseous microembolic signature, is similar to that reported by Smith et al. (1997) and Girault et al. (2010). d) Rapid change in the FM on a small percentage of the signal duration (microbubble near the upper artery wall). FMI evaluated in the accelerating phase was  $\Delta_f/\Delta_t = 500/0.016 = 31\text{kHz/s}$ .